A novel TIR-derived three-source energy balance model for estimating daily latent heat flux in mainland China using an all-weather land surface temperature product☆

Junming Yang [a], Yunjun Yao [a,*], Changliang Shao [b,*], Yufu Li [c], Joshua B. Fisher [d], Jie Cheng [a], Jiquan Chen [e], Kun Jia [a], Xiaotong Zhang [a], Ke Shang [a], Ruiyang Yu [a], Xiaozheng Guo [a], Zijing Xie [a], Lu Liu [a], Jing Ning [a], Lilin Zhang [f]

[a] State Key Laboratory of Remote Sensing Science, Faculty of Geographical Science, Beijing Normal University, Beijing 100875, PR China
[b] Institute of Agricultural Resources and Regional Planning, Chinese Academy of Agricultural Sciences, Beijing 100081, PR China
[c] Jincheng Meteorological Administration, Jincheng 048026, PR China
[d] Schmid College of Science and Technology, Chapman University, 1 University Drive, Orange, CA 92866, USA
[e] Department of Geography, Environment, and Spatial Sciences, Michigan State University, East Lansing, MI 48823, USA
[f] Faculty of Geo-Information and Earth Observation (ITC), University of Twente, 7500 AE Enschede, The Netherlands

ARTICLE INFO

ABSTRACT

A reliable thermal-derived method for spatially and temporally continuous latent heat flux (LE) estimates is vital for agricultural water resource management. In this study, we proposed a novel three-source LE model (TSLEM) derived by all-weather thermal infrared (TIR) land surface temperature (LST) to generate all-sky daily LE in mainland China. In this approach, LE was partitioned into the energy fluxes from canopy transpiration, soil evaporation, and interception water evaporation, respectively. Importantly, a new strategy was used to decompose radiational temperature into soil temperature (T_s), canopy temperature (T_c) and interception water temperature (T_i). Then soil evaporation was estimated by Penman-Monteith (PM) equation that parameterizes a soil resistance as a function of the normalized difference temperature index (NDTI) derived from T_s. A simplified MOD16 algorithm framework was used to estimate canopy transpiration and a Priestley-Taylor (PT) model to estimate interception evaporation. The proposed method was validated using 26 eddy covariance (EC) tower sites in mainland China across various vegetation types and applied to generate spatial continuous daily LE in mainland China. The results show that TSLEM accurately yielded daily LE with an average coefficient of determination (R^2) of 0.53 ($p{<}0.01$) and root-mean-square-error (RMSE) of 27.37 W/m^2, indicating TSLEM is a promising method for generating daily LE using all-weather LST at the regional scale.

1. Introduction

Terrestrial latent heat flux (LE), refers to the flux of water transferred from the land surface to the atmosphere by vegetation transpiration, soil evaporation, and interception evaporation, is a critical variable for many applications, such as crop yield forecast, drought monitor, and global climate change research (Fisher et al., 2017; Li et al., 2009; Zhou et al., 2021, 2020). Ground eddy-covariance (EC) tower measurements can provide accurate LE values from the scale of a few dozen meters to

approximately 1 km over several decades (Baldocchi et al., 2001; Liu et al., 2011; Tang et al., 2010). However, sparse EC towers can only represent limited local processes, and it is difficult to characterize regional or global scales due to terrestrial ecosystem heterogeneity and the complex dynamic nature of water, heat, and energy transfer processes (Kalma et al., 2008; Schimel et al., 2019; Yao et al., 2017a). Fortunately, remote sensing (RS) can provide spatially continuous and temporally regular measurements of terrestrial variables, such as land surface temperature (LST) and vegetation index (VI), for regional or

global LE estimation (Brust et al., 2021; Yao et al., 2018).

RS-derived LST is a critical variable for regional LE estimation due to its fast response to the variation of soil moisture (SM), which constrains canopy transpiration and soil evaporation (Carlson et al., 1994; Kalma et al., 2008; Sandholt et al., 2002). Many LST products derived from thermal infrared (TIR) satellite data, such as MODerate Resolution Imaging Spectroradiometer (MODIS), can provide frequent coverage and high spatial resolution inputs for LE models. However, LST information missed under cloudy conditions seriously limits spatially continuous and temporally regular monitoring of regional or global LE. Fortunately, various processes have been developed to compensate for missing information in MODIS LST by blending TIR-derived LST and microwave brightness temperature, thereby providing spatiotemporally continuous precise LST products for LE estimation (Duan et al., 2017; Xu and Cheng, 2021).

Over the last few decades, LST-derived surface energy balance (SEB) models have been widely used to estimate regional LE. One-source SEB models consider the land surface as "one-leaf" to calculate sensible heat flux (H) and LE, which may yield significant errors in partially vegetated landscapes (Verhoef et al., 1997; Yao et al., 2017b). To solve this defect, two-source SEB models decompose LST into soil temperature (T_s) and canopy temperature (T_c) to calculate H and then LE of soil and canopy (Anderson et al., 1997, 2007; Colaizzi et al., 2014, 2012; Kustas and Norman, 1999; Norman et al., 1995). However, two-source SEB models do not consider the influence of interception water from rainfall in LST decomposition and flux division. Previous studies reported that approximately 30% of rainfall can be intercepted in the evergreen beech forest (EBF) of New Zealand (Rowe, 1983). Similarly, approximately 6% and 11% of rainfall can be intercepted in Indonesia's logged and unlogged forests, respectively (Asdak et al., 1998). Considering the effect of interception water is crucial when estimating LE over a regional or global scale because interception water can affect the energy distribution and LST change via partial energy absorption.

In addition, the calculation of H is based on resistance-temperature gradient in SEB model. There are two problems that have not been fully solved. Firstly, resistance is parameterized by the complex theory of wind-profile and surface roughness length (Norman et al., 1995; Yao et al., 2017b). The complex resistance parameterizations generally lead to great uncertainty in LE estimation (Zhao et al., 2020). Secondly, the estimation of H is sensitive to the error of LST (Timmermans et al., 2007). Generally, more than 50% of errors are caused by the usage of LST in SEB models (Mu et al., 2011; Stewart et al., 1994). In contrast, many LST-derived methods have been developed to characterize the surface water conditions for LE estimation. Compared with SEB models, these methods are insensitive to LST errors. These include methods based on space features between LST and VI (LST-VI space methods) (Carlson et al., 1994), the water deficit index (WDI) (Moran et al., 1994), the crop water stress index (CWSI) (Jackson et al., 1981), the temperature-vegetation dryness index (TVDI) (Sandholt et al., 2002), and the normalized difference temperature index (NDTI) (McVicar and Jupp, 1998). An overview of LE models based on these methods was summarized in the Table S1, including their major merits and limitations. Overall, LST-VI space methods are widely used to estimate regional LE, yet the determining of dry/wet edges is subjectivity and the absence of one condition in the given images, very dry, very wet, fully vegetated, and bare surfaces may lead to large uncertain in the LE estimation. Although many methods, such as WDI, TVDI, CWSI, and NDTI, synergistic utilize satellite and meteorological data to determine the theoretical wet/dry edges, it is not operational on large scale due to the complex scheme and errors from too many input variables.

To overcome the above problems, we proposed a novel three-source LE model (TSLEM) driven by an all-weather LST product to estimate all-sky daily LE. We developed LE models by (i) considering the effect of interception water on energy balance model and LST decomposition; (ii) employing Penman-Monteith (PM) model, simplified MOD16 framework, and Priestley-Taylor (PT) model to calculate LE of soil, canopy

and interception water, respectively; (iii) developing a robust new strategy to calculate NDTI and then using NDTI to parameterize soil resistance in PM equation; and (iv) applying an all-weather LST product to drive the TSLEM model for LE estimation. The proposed method was compared with the two-source energy balance (TSEB) model, Priestley-Taylor-Jet Propulsion Laboratory (PT-JPL) model, and the double source LE model (DSLEM) at 26 flux tower sites across mainland China. Section 2 present the description of four models. The forcing variables and implementation of four models are described in Section 3. Results are given in Section 4, followed by a discussion in Section 5 and a conclusion in Section 6.

2. Methods

2.1. The description of TSLEM

TSLEM includes four modules: (1) a novel three-source energy balance model framework that considers the effect of interception water on LST decomposition and energy balance; (2) a Penman-Monteith (PM) model for LE_s estimation; (3) a simplified MOD16 framework for LE_c estimation; and (4) a Priestley-Taylor (PT) model for LE_i estimation. These four modules are introduced in the following sections.

2.1.1. A novel three-source energy balance model framework

In our model, the surface flux is divided into soil, canopy and interception water three components (Fig. 1). The LE is composed of soil (LE_s, W/m^2), canopy (LE_c, W/m^2) and interception water (LE_i, W/m^2) three components.

$$LE = LE_c + LE_s + LE_i \tag{1}$$

The available energy is partitioned into soil, canopy and interception water based on vegetation fractional coverage (f_c, unitless) and relative surface wetness (f_{wet}, unitless).

$$A_s = (1 - f_{wet})(1 - f_c) \times R_n - G \tag{2}$$

$$A_c = (1 - f_{wet}) \times f_c \times R_n \tag{3}$$

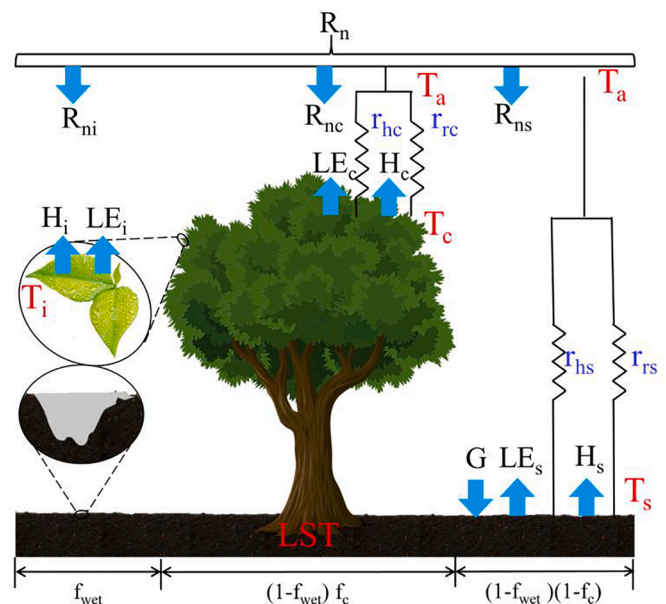$$A_i = f_{wet} \times R_n \tag{4}$$

Fig. 1. Schematic diagrams of parallel resistance and flux components for the novel three-source energy balance model framework. The symbols in the diagrams are defined in Section 2.1.

where A_s (W/m^2), A_c (W/m^2), and A_i (W/m^2) are the available energy of the soil, canopy, and interception water, respectively; G (W/m^2) is soil heat flux that can be calculated by the following equations,

$$G = R_n[(m-n)(1-f_c)(1-f_{wet})+n] \tag{5}$$

$$f_{wet} = \begin{cases} 0 & RH < 70\% \\ RH^4 & RH \geq 70\% \end{cases} \tag{6}$$

where RH (%) is relative humidity; m and n are empirical values and set as 0.315 and 0.05 (Kustas and Daughtry, 1990; Su, 2002), respectively. The reasonable representation of Eq. (6) has been proved by Stone et al. (1977) based on observed precipitation. In our model, there is no soil heat interaction between atmosphere and soil if the land surface is fully covered with interception water.

Here, the energy balance model of three components can be expressed as:

$$R_{ns} = LE_s + H_s + G \tag{7}$$

$$R_{nc} = LE_c + H_c \tag{8}$$

$$R_{ni} = LE_i + H_i \tag{9}$$

where R_{ns}, R_{nc}, and R_{ni} (W/m^2) are the net radiation of soil, canopy and interception water, respectively; H_s, H_c, and H_i (W/m^2) are the sensible heat fluxes of the soil, canopy, and interception water, respectively.

We assume the sensible heat flux from the soil and canopy surfaces are paralleled (Fig. 1), in which H_s and H_c can be calculated by Eq. (10) and Eq. (11).

$$H_s = \rho C_p \frac{T_s - T_a}{r_{as}} \tag{10}$$

$$H_c = \rho C_p \frac{T_c - T_a}{r_{ac}} \tag{11}$$

where ρ (kg/m^3) is the air density; C_p (J/kg/K) is the specific heat capacity of air; T_a (K) is the air temperature; T_s (K) and T_c (K) are the temperatures of the soil and canopy, respectively. Here, we consider the effect of interception water temperature (T_i (K)) on LST and propose a new strategy to calculate T_s and T_c (Text S1). r_{as} (s/m) in Eq. (10) is the total aerodynamic resistance that determines the ability of water vapor and heat from the soil surface transfer into the air above; The r_{as} is generally estimated by the classical theory of dynamic roughness and wind profile, but complex parameterization schemes and too many input variables may lead to uncertainty (Zhao et al., 2020). Based on the methods revised by Yao et al. (2017b), here r_{as} (s/m) (Eq. (12), Fig. 1) is parallel to convective heat transfer resistance (r_{hs} (s/m)) and radiative heat transfer resistance (r_{rs} (s/m)) in the soil surface (Choudhury et al., 1998; Mu et al., 2007).

$$r_{as} = \frac{r_{rs} \times r_{hs}}{r_{rs} + r_{hs}} \tag{12}$$

$$r_{rs} = \frac{\rho C_p}{4.0 \times \sigma \times T_a^3} \tag{13}$$

$$r_{hs} = \frac{107.0}{\frac{101.3}{P_a} \times \left(\frac{T_a}{293.15}\right)^{1.75}} \tag{14}$$

Where σ (W/m^2/K) is the Stefan–Boltzmann constant; P_a (KPa) is the atmospheric pressure. r_{ac} (s/m) in Eq. (11) is the aerodynamic resistance of water vapor and heat from the canopy surface transfer into the air above the canopy surface. As the MOD16 algorithm (Mu et al., 2011), in the current study, r_{ac} (Eq. (15), Fig. 1) is calculated as the parallel of radiative heat resistance (r_{rc} (s/m)) and convective resistance (r_{hc} (s/m)) in the canopy surface.

$$r_{ac} = \frac{r_{rc} \times r_{hc}}{r_{rc} + r_{hc}} \tag{15}$$

$$r_{hc} = \frac{1.0}{gl\_bl} \tag{16}$$

$$r_{rc} = \frac{\rho C_p}{4.0 \times \sigma \times T_a^3} \tag{17}$$

where gl_bl (m/s) is the leaf-scale boundary layer conductance, whose value is equal to the conductance of leaf to H (gl_sh (m/s)) per unit LAI (Mu et al., 2011). To make the method suitable for all ecosystems and reduce the model input variables. In the current study, gl_sh is set as 0.04 for all ecosystem types.

2.1.2. Penman–Monteith model for LE_S estimation

In our model, the fundamental method for estimating instantaneous LE_s is based on the PM equation,

$$LE_s = \frac{\Delta A_s + (1 - f_c)\rho C_p \times VPD/r_{as}}{\Delta + \gamma(1 + r_s/r_{as})} \tag{18}$$

where Δ (kPa/K) is the slope of the saturated vapor pressure (e_{sat} (kPa)) curve to temperature; VPD (kPa) is the water vapor pressure deficit; r_s (s/m) is a metric of the total factor that constrains water from soil transport to the atmosphere near the soil surface, which is mainly determined by surface SM availability. Therefore, it is necessary to utilize surface SM available to parameterize r_s. Here, r_s is parameterized using NDTI proposed by McVicar and Jupp (1998).

NDTI is strongly related to SM availability and can be calculated by TIR-derived LST and meteorological parameters.

$$NDTI = \frac{T_{smax} - T_s}{T_{smax} - T_{smin}} \tag{19}$$

where T_{smax} is the modeled soil surface temperature when the soil surface resistance is infinite, and T_{smin} is the modeled soil surface temperature when the soil surface resistance is close to zero. T_{smax} and T_{smin} can be taken as the physically limited soil surface temperatures under given meteorological conditions (McVicar and Jupp, 1998). T_s close to T_{smin} is an indication of wetness, while T_s close to T_{smax} is an indication of dryness. Therefore, NDTI can be used to indicate soil surface moisture conditions.

McVicar and Jupp (1998) calculated T_{smax} and T_{smin} in Eq. (19) by inversion of the one-layer or two-source resistance energy balance model (REBM). In our study, T_{smax} and T_{smin} are calculated by the following revised method. By combining Eqs. (7), (10), and (18), we can obtain Eq. (20),

$$T_s = \frac{r_{as} \times A_s}{\rho C_p} \times \frac{\gamma(1 + r_s/r_{as})}{\Delta + \gamma(1 + r_s/r_{as})} - \frac{(1 - f_c) \times VPD}{\Delta + \gamma(1 + r_s/r_{as})} + T_a \tag{20}$$

For dry bare soil with no available water, where $r_s=\infty$, the soil temperature reaches its highest value. In this case, the soil temperature can be expressed as Eq. (21). The soil temperature reaches its lowest value for well-watered soil, where r_s is very small. In this case, the soil temperature can be expressed as Eq. (22).

$$T_{smax} = \frac{r_{as} \times A_s}{\rho C_p} + T_a \tag{21}$$

$$T_{smin} = \frac{r_{as} \times A_s}{\rho C_p} \times \frac{\Delta}{\Delta + \gamma} - \frac{(1 - f_c) \times VPD}{\Delta + \gamma} + T_a \tag{22}$$

NDTI and r_s have the following relationship: (i): r_s decrease with the increase of NDTI; (ii): r_s is infinity when NDTI is close to zero. Based on the relationship between them, we assume there is an inverse relationship between r_s and NDTI (Fig. 2) which can be expressed as Eq. (23).
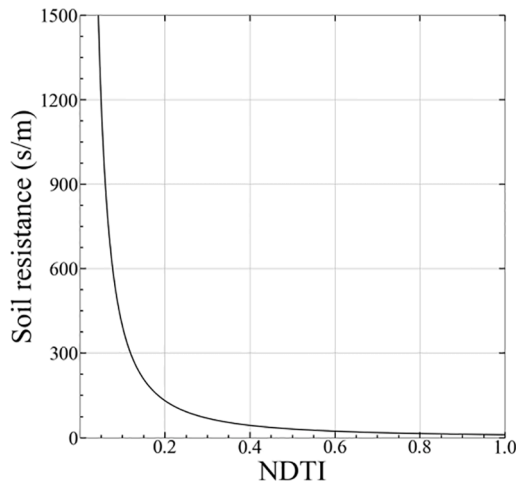
Fig. 2. The relationship between NDTI and soil resistance.

$$r_s = \frac{C_k}{NDTI^{n_k}} \tag{23}$$

where C_k and n_k are the empirical parameters and set as 10.0 and 1.6, respectively in this study.

2.1.3. Simplified MOD16 framework for LE_c estimation

Here, a simplified MOD16 algorithm is implemented to calculate instantaneous LE_c,

$$LE_c = \frac{\Delta A_c + \rho C_p \times VPD \times f_c / r_{ac}}{\Delta + \gamma(1 + r_c / r_{ac})} \tag{24}$$

where r_c is the effective resistance to transpiration from the plant, which is highly dependent on environmental conditions (VPD, T_a, carbon dioxide concentration, water potential, etc.) and vegetation growth status (Mu et al., 2007, 2011). To reduce the error caused by too many input variables, we use the invariant parameters proposed by Yao et al. (2017a) to calculate r_c, such that:

$$r_c = 1/C_c \tag{25}$$

$$C_s = cL \times m(T_a) \times m(VPD) \tag{26}$$

$$C_c = C_s \times LAI \tag{27}$$

where cL (m/s/K/Pa)) is the mean surface conductance per unit LAI, in our model, cL is set as 0.0022 (Cleugh et al., 2007); C_c (m/s) is the canopy conductance; and C_s (m/s) is the stomatal conductance. $m(T_a)$ is calculated with an optimum air temperature (T_{opt}) set as 298.15 K (Fisher et al., 2008); m(VPD) is calculated by setting VPD_{open} to 0.65 kPa and VPD_{close} to 2.9 kPa (Yao et al., 2017a).

$$m(T_a) = \exp\left[-\left(\frac{T_a - T_{opt}}{T_{opt}} \right)^2 \right] \tag{28}$$

$$m(VPD) = \begin{cases} 1.0 & VPD \le VPD_{open} \\ \dfrac{VPD_{close} - VPD}{VPD_{close} - VPD_{open}} & VPD_{close} < VPD < VPD_{open} \\ 0.1 & VPD \ge VPD_{close} \end{cases} \tag{29}$$

2.1.4. Priestley-Taylor model for LE_i estimation

The Priestley-Taylor (PT) (1972) model is used to estimate LE_i based on A_i (Fisher et al., 2008, 2011; Priestley and Taylor, 1972; Wang et al., 2019).

$$LE_i = \alpha \frac{\Delta}{\Delta + \gamma} A_i \tag{30}$$

where α is the PT parameter (1.26).

2.2. Daily LE estimation

Satellite-derived LE values from the TSLEM model are instantaneous, and we upscale instantaneous LE into daily values via the invariant evaporative fraction (EF) method (Sugita and Brutsaert, 1991),

$$EF_{inst} = \frac{LE_{inst}}{Rn_{inst} - G_{inst}} = EF_{daily} \tag{31}$$

$$LE_{daily} = EF_{daily}(Rn_{daily} - G_{daily}) \tag{32}$$

where EF_{inst} (unitless) is an instantaneous EF; EF_{daily} (unitless) is a daily EF; LE_{inst} (W/m^2) is instantaneous LE; LE_{daily} (W/m^2) is daily LE; Rn_{inst}-G_{inst} (W/m^2) is instantaneous available energy, and Rn_{daily}-G_{daily} (W/m^2) is daily available energy.

2.3. Comparison with other LE models

2.3.1. Double-source LE model (DSLEM)

The framework of DSLEM is similar to TSLEM except DSLEM separates LE into LE_c and LE_s two components. The calculations of LE_c and LE_s are similar to those of TSLEM. The DSLEM model can be written as:

$$LE = LE_c + LE_s \tag{33}$$

$$A_c = R_n \times f_c \tag{34}$$

$$A_s = R_n(1 - f_c) - G \tag{35}$$

$$LE_c = \frac{\Delta A_c + \rho C_p \times VPD / r_{ac}}{\Delta + \gamma(1 + r_c / r_{ac})} \tag{36}$$

$$LE_s = \frac{\Delta A_s + \rho C_p \times VPD / r_{as}}{\Delta + \gamma(1 + r_s / r_{as})} \tag{37}$$

The calculation of r_{as}, r_{ac}, and r_c refers to Eqs. (12), (15), and (25). The parametrization scheme of r_s is similar to TSLEM except that DSLEM decomposes LST into T_s and T_c.

2.3.2. Two-source energy balance (TSEB) model

The originally TSEB model was developed by Norman et al. (1995) and has been revised by Kustas and Norman (1999). TSEB assumes that the available energy is equal to turbulent fluxes and partitions net radiation into canopy and soil components (Eq. (38)).

$$R_n = R_{nc} + R_{ns} = LE + H + G \tag{38}$$

The LE of each component is calculated as the residual of energy balance models.

$$R_{nc} = LE_c + H_c \tag{39}$$

$$R_{ns} = LE_s + H_s + G \tag{40}$$

Here, H_c and H_s are calculated by series resistance network form, which can be expressed as follows:

$$H = \rho C_p \frac{T_{ac} - T_a}{r_a} \tag{41}$$

$$H_c = \rho C_p \frac{T_c - T_{ac}}{r_x} \tag{42}$$

$$H_s = \rho C_p \frac{T_s - T_{ac}}{r_s} \tag{43}$$

where T_{ac} (K) is the air temperature within the canopy boundary layer and r_x (s/m) is the resistance in the boundary layer near the canopy. Satellite-derived radiometric temperature is the composition of T_s and T_c. TSEB model calculates the initial T_s and T_c from the following equation.

$$T_c = T_a + \frac{R_{nc} \times r_a}{\rho C_p} \left(1 - \alpha \times f_c \times \frac{\Delta}{\Delta + \gamma} \right) \tag{44}$$

$$LST^4 = f_c \times T_c^4 + (1 - f_c) \times T_s^4 \tag{45}$$

2.3.3. Priestley-Taylor-based LE model (PT-JPL)

The PT-JPL model developed by Fisher et al. (2008) was downscaled the potential LE to actual LE by multiple eco-physiological constraint functions. The model can be described as:

$$LE = LE_s + LE_c + LE_i \tag{46}$$

$$LE_s = [f_{sm}(1 - f_{wet}) + f_{wet}] \times \frac{\Delta}{\Delta + \gamma} \times \alpha \times (R_{ns} - G) \tag{47}$$

$$LE_c = (1 - f_{wet}) \times f_g \times f_T \times f_M \times \alpha \frac{\Delta}{\Delta + \gamma} R_{nc} \tag{48}$$

$$LE_i = f_{wet} \times \alpha \frac{\Delta}{\Delta + \gamma} R_{ni} \tag{49}$$

where f_{sm} is the soil moisture constraint; f_g is the green canopy fraction; f_T is the plant temperature constraint, and f_M is the plant moisture constraint.

3. Data processing and implementation of LE models

3.1. Eddy-Covariance data

Eddy-Covariance (EC)-measured water and heat fluxes and the corresponding meteorological data across mainland China were used to evaluate the model performance. EC data from 26 sites (Fig. 3, Table S2) were provided by the chinese ecosystem research network (CERN) (Fu et al., 2010), synergetic enhanced observation network (SEON) for northern China, flux sites of the Haihe River Basin (Haihe-flux) (Liu et al., 2013), Chinaflux (Yu et al., 2006) and Fluxnet (Pastorello et al., 2020). These sites cover major vegetation types across China, including cropland (CRO, 9 sites), deciduous needle forest (DNF, 1 site), evergreen broadleaf forest (EBF, 1 site), evergreen needleleaf forest (ENF, 1 site), grassland (GRA, 11 sites), open shrublands (OSH, 1 site), mixed forest (MF, 1 site), and wetland (WET, 1 site). The climate zones covered by these EC towers include the temperate monsoon climate (TeMC), temperature continental climate (TeCC), subtropical monsoon climate (SuMC), and plateau mountain climate (PlMC). The distinctive characteristics of these sites are suitable to evaluate the model performance. The corresponding meteorological and heat flux measurements include net radiation (R_n), incident solar radiation (R_s), latent heat flux (LE), sensible heat flux (H), air temperature (T_a), soil temperature (T_s), atmospheric pressure (P_a), relative humidity (RH), soil moisture (SM), and wind speed (WS). The daily parameters were set as null when more than 25% of the half-hourly data are missing. Because the EC data suffer a problem of energy imbalance in which the total observed LE and H are generally less than available energy. Therefore, LE here was corrected using the method developed by Twine et al. (2000) (Eq. (50)).

$$LE_{cor} = \frac{R_n - G}{H_{uncor} + LE_{uncor}} \times LE_{uncor} \tag{50}$$
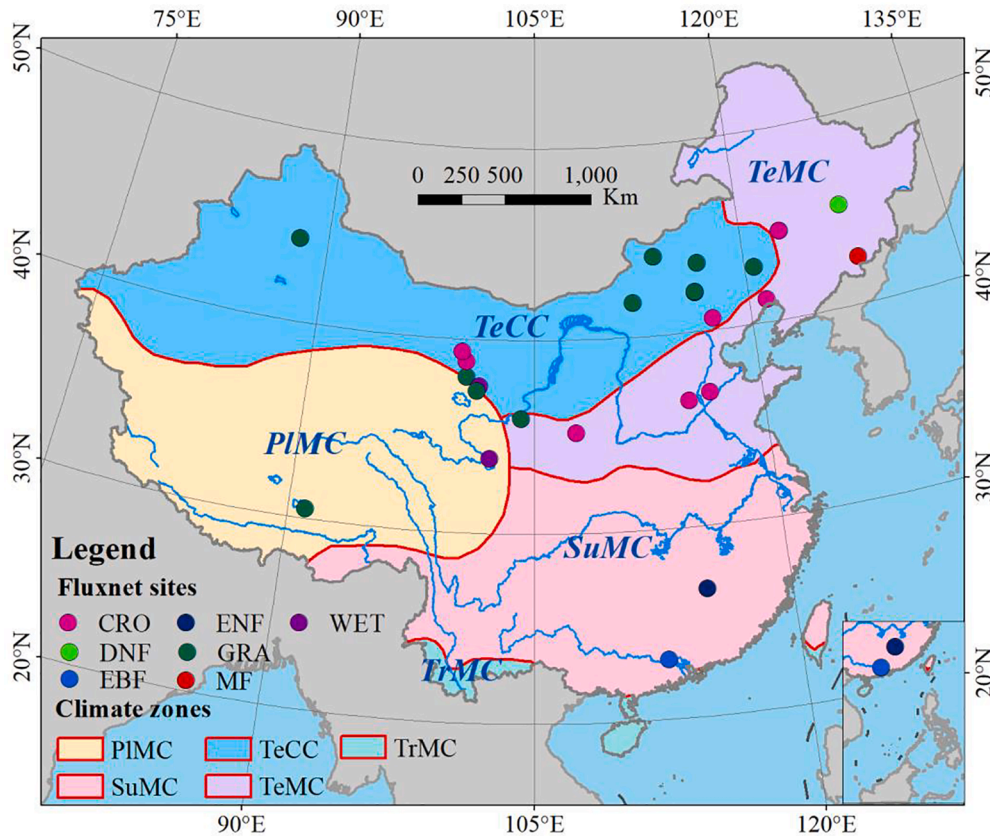

Fig. 3. Locations and climate zones of selected EC sites over China. The climatic zones are the temperate monsoon climate (TeMC), temperature continental climate (TeCC), plateau mountain climate (PlMC), subtropical monsoon climate (SuMC), and tropical monsoon climate (TrMC).

where LE_{cor} is corrected LE; LE_{uncor} and H_{uncor} are uncorrected LE and H, respectively.

3.2. Satellite and reanalysis datasets

Datasets used in the LE model here are listed in Table 1. These datasets include the blended all-weather instantaneous LST, leaf area index (LAI), fractional vegetation cover (f_c), and meteorological data. The instantaneous LST product required for characterizing soil surface moisture conditions was provided by Duan et al. (2017) with a 1 km spatial resolution. The all-weather LST was generated by blending TIR-derived MYD11A1 LST and PMW-derived AMSR-E LST. Both TIR and AMSR-E sensors are aboard the Aqua satellite and the cross equator at 1:30 am/pm (Duan et al., 2017). We also used 8-day Global land surface satellite (GLASS) f_c and LAI products with a spatial resolution of 1 km (Jia et al., 2015; Liang et al., 2021; Xiao et al., 2014).

Instantaneous and daily gridded meteorological data were derived from Modern-Era Retrospective Analysis for Research and Applications, version 2 (MERRA-2) developed under the National Aeronautics and Space Administration (NASA) Modeling Analysis and Prediction Program (Gelaro et al., 2017). Here, we used R_s, surface net downloads longwave radiation (R_l), P_a, T_a, and RH at 6:00 UTC (approximately 14:00 local time in China, close to the Aqua satellite transit time) to derive instantaneous LE. Daily R_s and R_l were used to upscale instantaneous LE into daily values.

3.3. Implementation of LE models

The four models mentioned above estimated all-sky LE are validated by ground-based EC observations. The force variables of four LE models at sites include satellite data (f_c, LAI, and all-weather LST), canopy height, instantaneous (RH, R_n, R_s, T_a, P_a) and daily (R_n) meteorology data (Table 2). The EC data and the corresponding meteorology data were derived from in-situ observation and satellite data was derived from pixel values in the corresponding location of EC sites. We referenced the method proposed by Anderson et al. (2007) to set canopy height. Daily variables were linearly aggregated from half-hourly in-situ measurements. Here, the daily LE estimated by four models was upscaled from an instantaneous scale.

Table 1
Description of the datasets used in this study.

Variables	Datasets	Units	Temporal/spatial resolution	Timespan	Reference
f_c	GLASS	No unit	8 day/1km	2002–2011	(Jia et al., 2015)
LAI	GLASS	No unit	8 day/1km	2002–2011	(Xiao et al., 2014)
LST	All-weather LST	K	Instantaneous/1km	2002–2011	(Duan et al., 2017)
RH	MERRA-2	%	Hourly/ 0.5°	2006–2008	(Gelaro et al., 2017)
T_a	MERRA-2	K	Hourly/ 0.5°	2006–2008	(Gelaro et al., 2017)
P_a	MERRA-2	K	Hourly/ 0.5°	2006–2008	(Gelaro et al., 2017)
R_s	MERRA-2	W/m²	Daily and Hourly/0.5°	2006–2008	(Gelaro et al., 2017)
R_l	MERRA-2	W/m²	Daily and Hourly/0.5°	2006–2008	(Gelaro et al., 2017)

Table 2
The force data of four LE models at the site scale.

Models	Input variables
DSLEM	R_n, P_a, T_a and RH, LST, f_c and LAI
TSLEM	R_n, P_a, T_a and RH, LST, f_c and LAI
TSEB	R_n, R_s, T_a, P_a, RH, LST, f_c, LAI, and canopy height
PT-JPL	R_n, P_a, T_a and RH, f_c and LAI

The forcing variables for mapping spatial continuous daily LE in mainland China based on TSLEM driven by satellite variables (all-weather LST, LAI, and f_c), instantaneous meteorological variables (T_a, R_s, R_l, RH, and P_a), and daily meteorological variables (R_s and R_l) from MERRA-2 data. To match the temporal and spatial resolution of all-weather LST, the MERRA-2 data were spatially interpolated to 1 km using the bilinear interpolation method, the 8-day f_c and LAI products were linearly interpolated into daily. All the above mentioned data processing procedure is implemented using the Python programming language.

4. Results

4.1. LST decomposition

Across all sites, decomposing LST into three components can improve the performance of T_s simulation under both aerodynamic resistance schemes of TSLEM and TSEB, with respective average R^2 of 0.81 and 0.84 ($p<0.01$), accompanying RMSE of 5.27 K and 5.48 K (Figs. 4 and 5). In contrast, decomposing LST into two components has lower performance under both aerodynamic resistance schemes of TSLEM [$R^2=0.77$ ($p<0.01$) and RMSE=7.39 K] and TSEB [$R^2=0.79$ ($p<0.01$) and RMSE=6.19 K]. Both decomposing LST into two and three components under the TSEB scheme are slightly better than those of TSLEM, with an average reducing RMSE of 1.20 K and 0.49 K and increasing R^2 values of 0.03 and 0.02 ($p<0.01$), respectively.

The performance of decomposing LST into two and three components is similar in arid sites (DL2 and SZWG) under two aerodynamic resistance parameterization schemes (Figs. 4 and 5). In contrast, in three sites with sufficient rainfall (CBS, DHS, and QYZ), decomposing LST into three components significantly improves the performance of T_s simulation under both TSLEM and TSEB parameterization schemes, with an average decrease in RMSE of 1.94 K and 2.06 K, and an increase in R^2 of 0.02 and 0.33 ($p<0.01$).

4.2. Model validation at EC sites

4.2.1. Validation of the estimated instantaneous LE

To evaluate our model, we first validated the estimated instantaneous LE using TSLEM against in-situ measurements at all-sky conditions. As illustrated in Fig. 6, the estimated instantaneous LE in general agrees with ground-based measurements over most sites, yielding an average R^2 of 0.39 ($p<0.01$), RMSE of 105.98 W/m², and bias of 44.22 W/m². But the significant overestimation at two arid GRA sites (DS and XLGL) indicates the application of TSLEM in arid grassland requires more caution.

TSLEM shows variable capability over different vegetation types and climate zones. TSLEM performs generally better in forests (including MF, DNF, EBF, and ENF), with an average R^2 of 0.54($p<0.01$) and RMSE of 97.79 W/m², followed by cropland, yielding an average R^2 of 0.37 ($p<0.01$), and RMSE of 108.38 W/m², and performs worst in the grass with R^2 of 0.28($p<0.01$) and RMSE of 113.52 W/m². In addition, TSLEM has good performance in the EC sites of plateau mountain climate (PlMC) and subtropical monsoon climate (SuMC), with respective average R^2 of 0.69 and 0.54 ($p<0.01$), accompanying RMSE of 73.94 W/m² and 101.05 W/m². In contrast, TSLEM performs poor in the EC sites
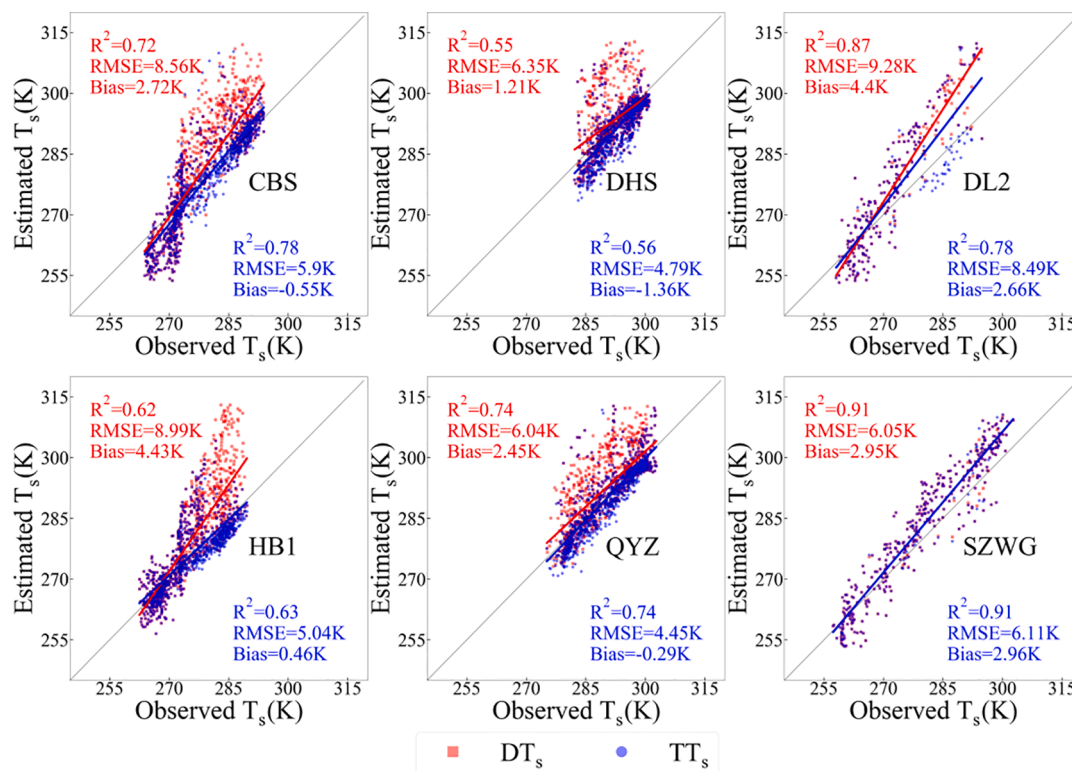
Fig. 4. Validation of DT_s and TT_s for the aerodynamic resistance parameterization scheme adopted by TSLEM at 6 sites (DT_s represent decomposing LST into the double source and TT_s represent decomposing LST into three sources).
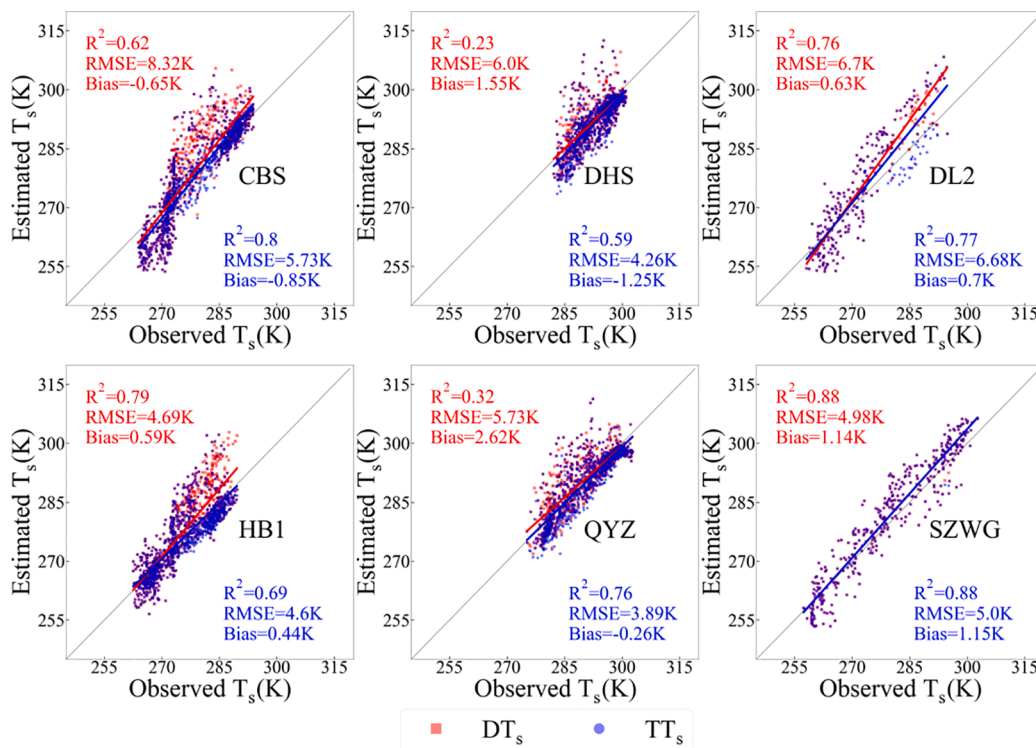

Fig. 5. Validation of DT_s and TT_s for the aerodynamic resistance parameterization scheme adopted by TSEB at 6 sites.

of temperate monsoon climate (TeMC) [$R^2=0.38$ ($p<0.01$) and RMSE=111.18 K] and temperate continental climate (TeCC) [$R^2=0.28$ ($p<0.01$) and RMSE=110.90 K].

4.2.2. Validation of the estimated daily LE

In general, TSLEM has a good capability to estimate daily LE in all-sky conditions, with an average R^2 of 0.53 ($p<0.01$), accompanied by an average RMSE of 27.37 W/m^2 and a bias of -6.49 W/m^2 (Fig. 7). The
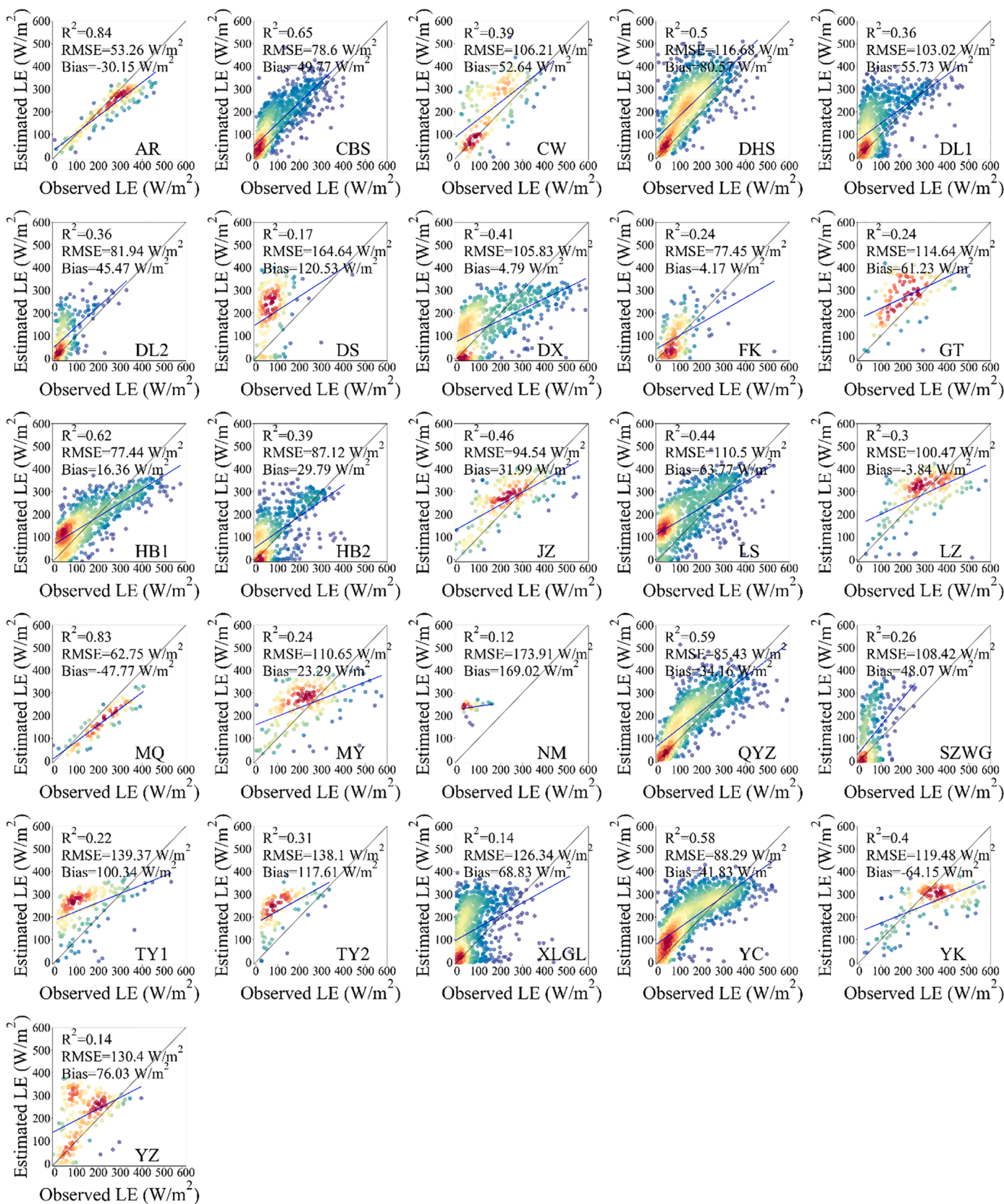
Fig. 6. Scatterplots of observed instantaneous LE versus TSLEM estimated instantaneous LE under all-sky conditions over 26 sites.
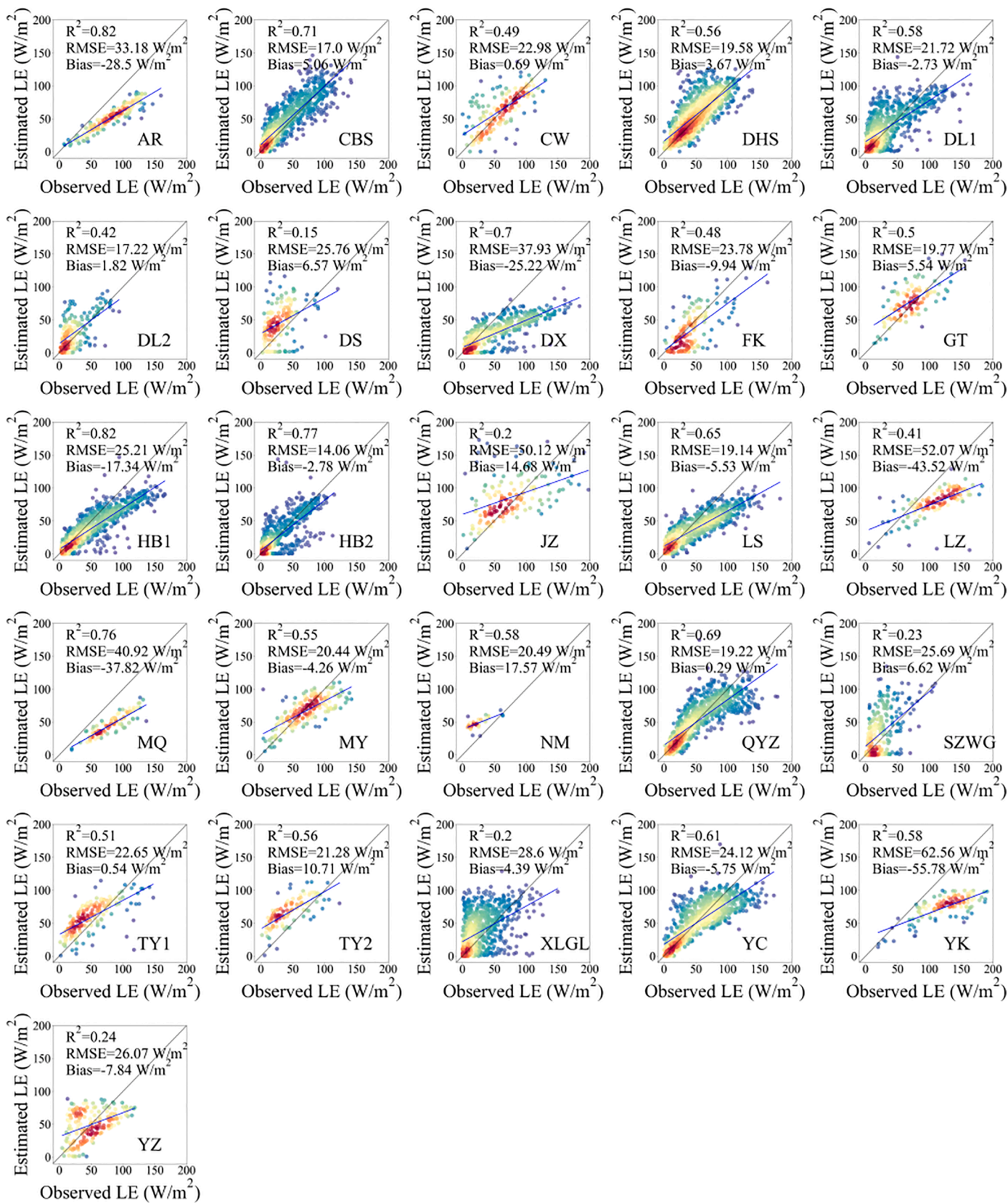
Fig. 7. Scatterplots between observed daily LE and TSLEM estimated daily LE over 26 sites.

absolute value of bias at all sites except LZ, MQ, and YK is less than 40 W/m^2 indicating the systematic bias of TSLEM is small. It is interesting to find the significant overestimate of instantaneous LE at two arid GRA sites (DS and XLGL) has been largely reduced on a daily scale.

The observed LE reaches its highest around July and August of summer and then decreases from summer to winter (Fig. 8). Generally, observed LE seasonal variations were well captured by TSLEM estimated LE at most sites. In addition, the amplitudes of TSLEM estimated LE is close to the observed at most sites. However, TSLEM tends to underestimate LE at some arid sites (AR, LZ, DX, MQ, and YK).

4.3. Comparison with other LE models

Across all sites (Fig. 9), TSLEM has the best performance against ground measurement among all four LE models, with a mean R^2 of 0.53

($p<0.01$), RMSE of 27.37 W/m^2, a bias of −6.49 W/m^2, and relative error (RE) of 6.02%. The TSEB model perform poor, suggesting a mean R^2 of 0.31 ($p<0.01$), RMSE of 42.67 W/m^2, a bias of 1.45 W/m^2, and RE of 11.13%. The performance of PT-JPL is similar to TSLEM, reproducing LE with a mean R^2 of 0.52 ($p<0.01$), RMSE of 28.10 W/m^2, bias of −12.85 W/m^2, and RE of −21.65%. The performance of DSLEM is significantly worse than TSLEM and PT-JPL but better than TSEB, suggesting an average R^2 of 0.45 ($p<0.01$), RMSE of 31.04 W/m^2, bias of −15.16 W/m^2 and RE of −24.29%.

We also compared the statistical distributions of four models estimated LE with ground observed LE. As shown in Fig. 10, the estimated LE from four LE models differs greatly despite the same forcing inputs. For almost all EC sites, the difference between observed and estimated LE is the least in TSLEM and is the largest in TSEB. The box of TSLEM is consistent with the observations except for LZ, MQ, NM, and YK EC sites.
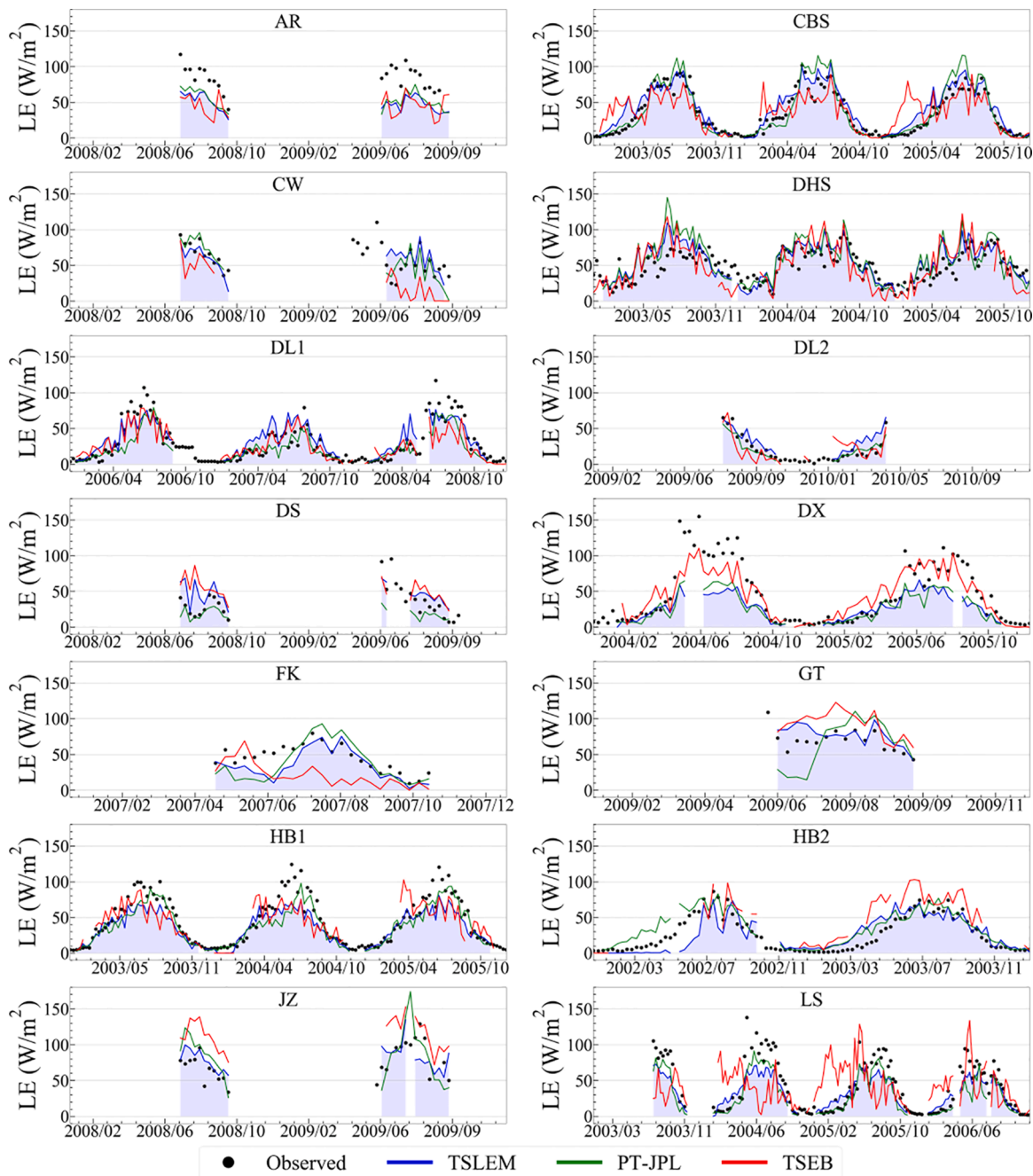

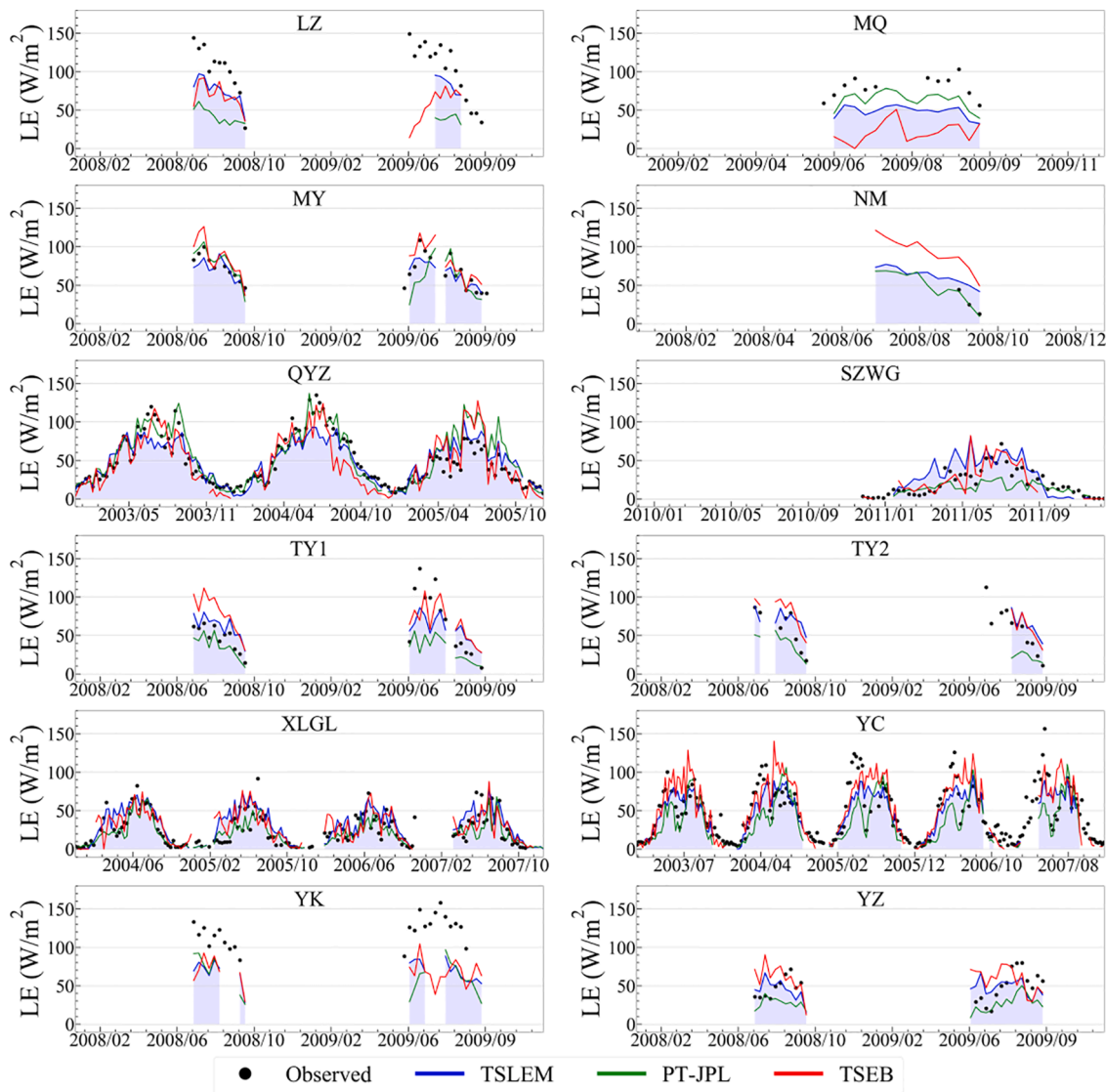Fig. 8. The 8-day time series observed and estimated daily LE (TSLEM, PT-JPL, and TSEB) over 26 EC sites.

Fig. 8. (*continued*).

The upper box boundaries of TSLEM are higher than those of DSLEM and closer to observations at almost all sites. The large amplitudes of the TSEB box and abundant outliner points indicate great uncertainty exists in the TSEB model. The shape and location of the PT-JPL box are similar to observations at humid sites. However, the box boundary of PT-JPL is lower than other models and observed in some arid and semiarid sites (DS, LZ, TY1, TY2, XLGL, and YZ).

4.4. Sensitivity analysis

The contribution of forcing variables to the TSLEM and TSEB output was evaluated by a simple relative sensitivity method (RSM) refer to Eq. (51) (Zhan et al., 1996). The relative sensitivity (RS_v) of each input variable v (LST, NDVI, RH, R_n, T_a, WS) was calculated by comparing the LE_0 estimated by the reference input variable with LE_v estimated by changing the input variable v. The sensitivity analysis was conducted by the data from DHS, DS, DX and GT on Day of Year (DOY) of 180, 244, 192 and 185, respectively, which cover four main climate zones of China. The RH was less than 70% (dry surface) in DS and GT, and greater than 70% (wet surface) in DHS and DX.

$$RS_v = \frac{LE_v - LE_0}{LE_0} \qquad (51)$$

As shown in Fig. 11, the sensitivity of TSLEM to R_n is determined to be the highest, and R_n is positively correlated with LE, which is common among many LE models (Fisher et al., 2009, 2017; Wang et al., 2019). As R_n increases from −20% to 20%, LE almost equally increases from −20% to 20%. The second-largest variation of TSLEM is caused by the change of RH on the wet surface, while caused by the change of T_a on the dry surface. When RH and T_a range from −20% to 20%, LE ranges from −19% to 26% for RH on wet surfaces and from −17% to 12% for T_a on dry surfaces. TSLEM is insensitive to the error of LST on wet surfaces, while the increase in LST generally results in the underestimation of LE on dry surfaces. The increase in LST by 10% and 20% would lead to a 6% and 20% underestimation of LE on dry surfaces, respectively. The sensitivity analysis result shows that the estimated LE is insensitive to the error of two vegetation parameters (f_c and LAI). The fluctuation of LE is less than 10% when the variation of f_c is within ±20%. A 20% variation in LAI only results in a 3% fluctuation of LE.

TSEB is most sensitive to variations in temperature (LST and T_a), especially on dry surfaces (DS and GT). T_a is positively related to LE, while LST is negatively related to LE. The change in LST of ±20% would result in variation in LE from −55% to 78% on the dry surface. LE varies from −40% to 36% when T_a changes within ±20%. TSEB is insensitive to the error of R_n, f_c, and LAI. A 20% variation in f_c, LAI, and R_n results in fluctuations in LE less than 2%, 4%, and 11%, respectively.
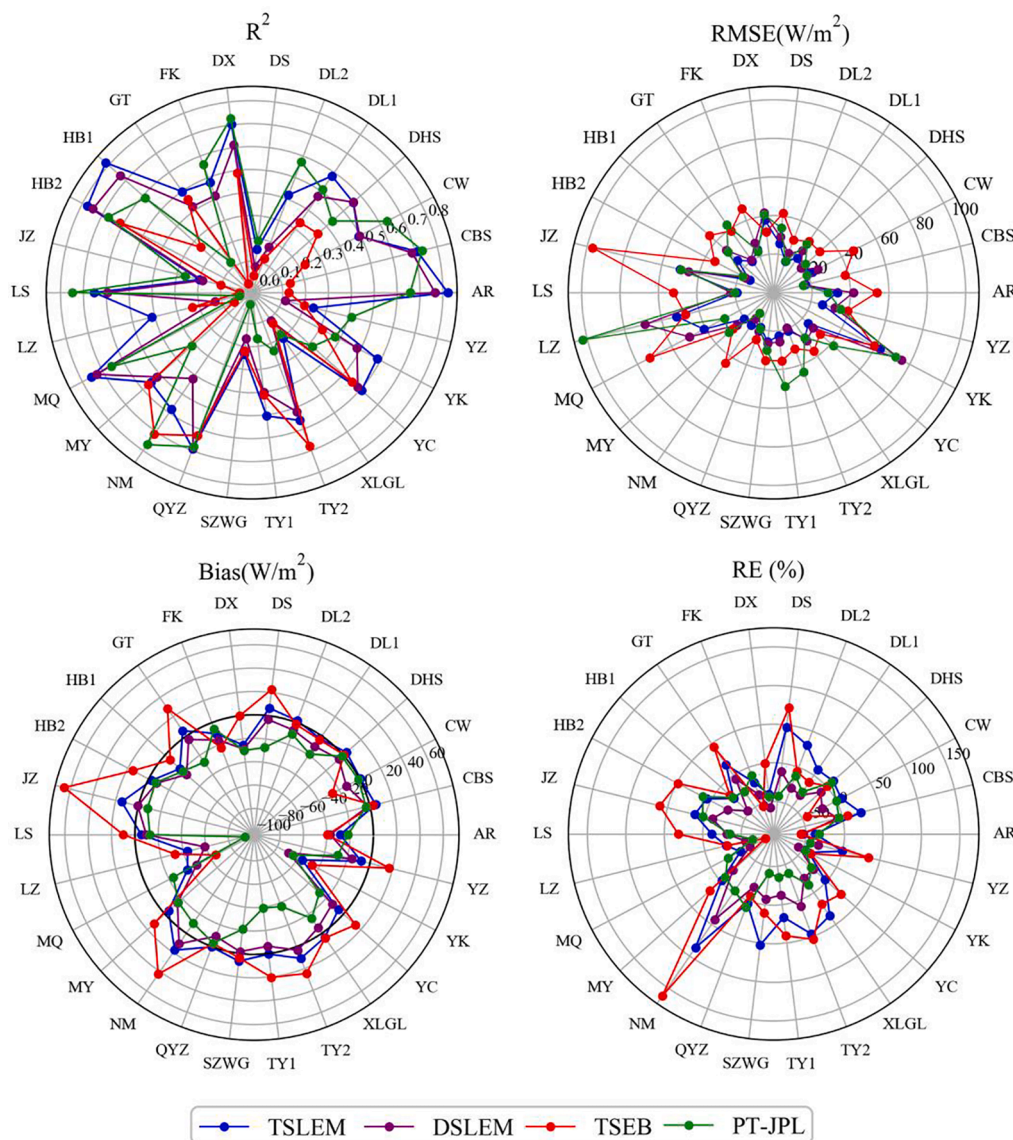
Fig. 9. Radar chart of four statistical metrics (R^2, RMSE, bias, and RE) for four models (TSLEM, DSLEM, PT-JPL, and TSEB) over 26 EC sites.

Overall, R_n and RH are the important error sources of TSLEM on wet surfaces, but R_n and T_a are the important error sources on dry surfaces. The increase in R_n would result in the overestimation of LE. TSEB is most sensitive to the errors of LST and T_a. The decrease in LST or increase in T_a would result in the overestimation of LE. TSLEM shows less sensitivity to LST than TSEB.

4.5. Mapping of daily LE across chinese landmass

The proposed model was employed to generate all-sky LE products during 2006–2008 over the Chinese landmass. The temporal variations of monthly LE show obvious seasonality (Fig. 12). The lowest LE occurs around December and January and then starts to increase. The LE reaches its highest value around July and then decreases to its lowest value. The major deserts of Northwest China remain consistently low, while the southern tropical monsoon climate zone remains consistently high over the year.

The spatial distribution of annual mean LE during 2006–2008 (Fig. 13) shows strong regional variations. The highest LE occurs in the tropical monsoon climate and subtropical monsoon climate zones (South and Central China), followed by the temperate monsoon climate zone (North and Northeast China), and the lowest LE occurs in the temperature continental climate and plateau mountain climate zones, including Qinghai-Tibet, Inner Mongolia, and Northwest China. The mean annual LE in China is 30.5 W/m², equal to 376.6 mm/year. The spatial pattern and magnitudes of LE are consistent with those of previous studies (Yao et al., 2013; Zhang et al., 2010).

5. Discussion

5.1. TSLEM improvements to other models

The biggest difference between the TSLEM and DSLEM is the division of flux. TSLEM segments LE into three components: LE_c, LE_s, and LE_i; while DSLEM segments LE into two components: LE_c and LE_s. The occurrence of interception water after rainfall causes DSLEM to incorrectly divide LE_i into LE_c and LE_s. The interception water is evaporated at potential evaporation (Fisher et al., 2008), while soil evaporation and canopy transpiration are constrained by environmental conditions and less than potential evaporation. Therefore, incorrect energy flux partition is responsible for the underestimation of DSLEM (Fig. 10). Consideration of interception water in the TSLEM improved the performance of LE estimation, with an increasing R^2 of 0.08, decreasing RMSE of 3.67 W/m², and decreasing bias of 8.67 W/m² (Fig. 9).
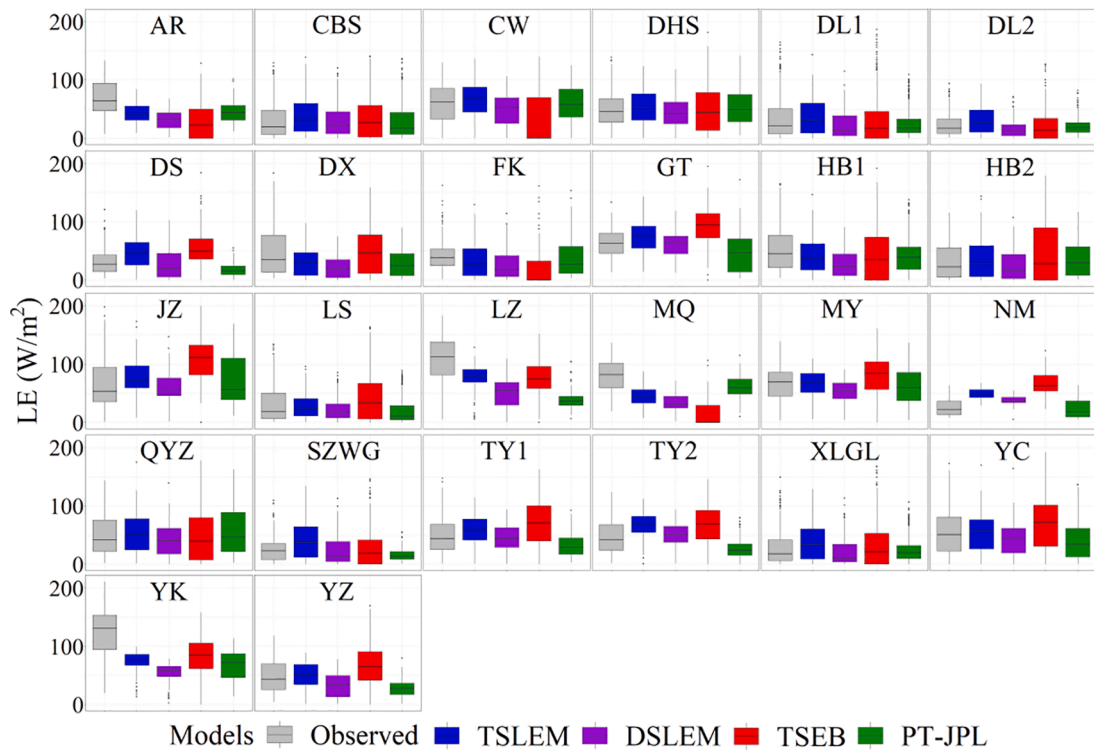
Fig. 10. Box plot of four models estimated LE and ground measured LE over 26 sites. The box plot shows the median (boxes centerline), 75%, and 25% (upper and lower box boundaries), and the possible outlier data point (the data greater than V75+1.5(V$_{75}$-V$_{25}$) or less than V$_{25}$–1.5(V$_{75}$-V$_{25}$), where V$_{25}$ and V$_{75}$ are values of 25% and 75%).
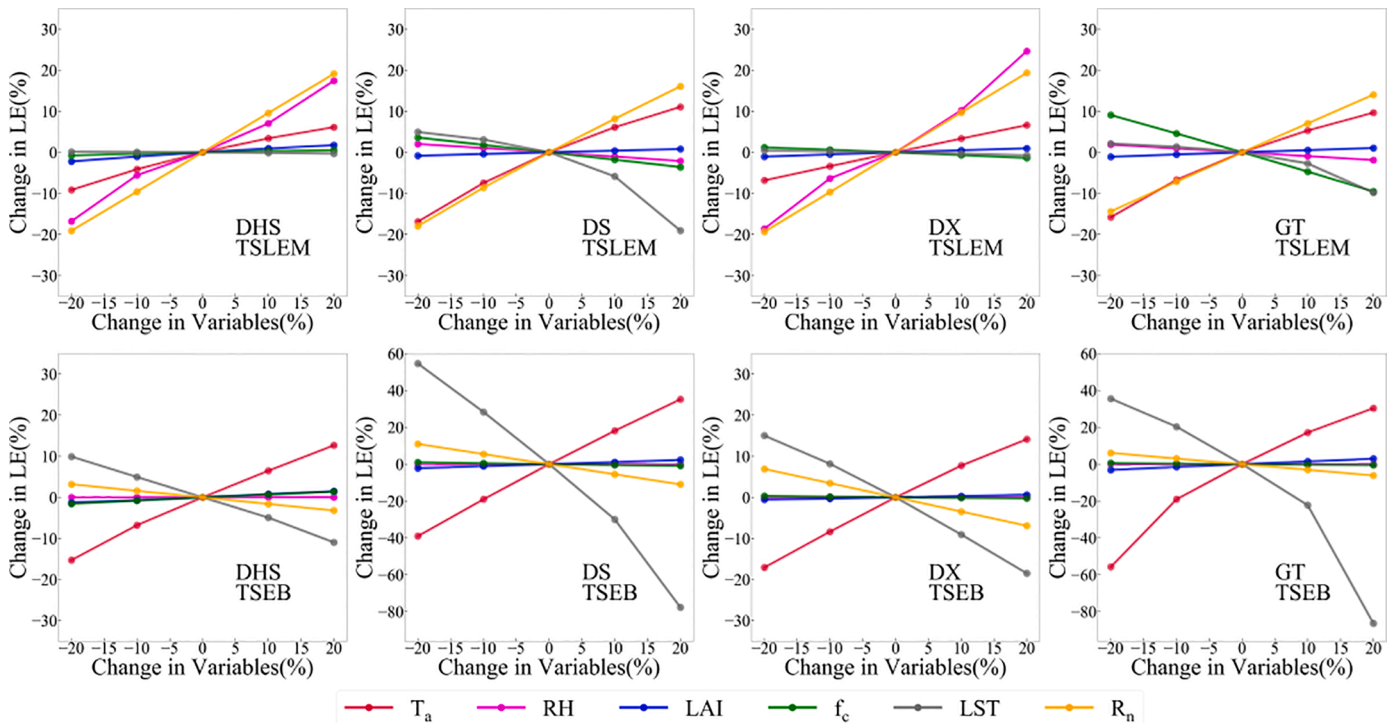

Fig. 11. Sensitivity analysis of TSLEM and TSEB at four sites to the errors of T$_a$, RH, LAI, f$_c$, LST, and R$_n$ from −20% to 20% and incrementing by 10%. (The Y-axis ranges of TSEB at DS and GT are different from others.).

TSEB requires knowledge of soil and canopy temperatures. However, the LST measured by the TIR sensor is the composite of the soil and canopy temperature. Therefore, we are required to decompose LST into canopy and soil temperature. The error in LST may cause significant uncertainty in LST decomposition and then cause uncertainty in H (Timmermans et al., 2007). To avoid the error caused by the calculation of H, TSLEM simulates LE directly based on the PM or PT equation. One advantage of this method is that it avoids errors in the component
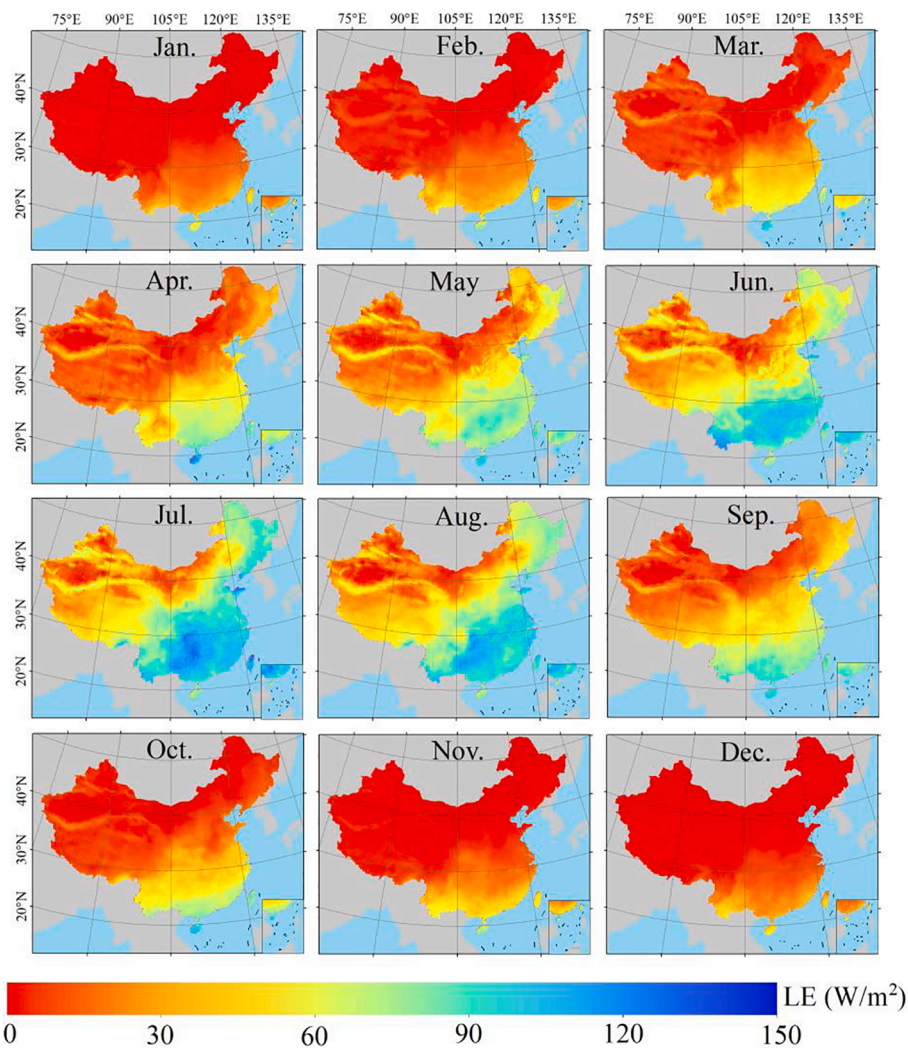
Fig. 12. The spatial distribution of monthly LE over mainland China from January to December during 2006–2008.
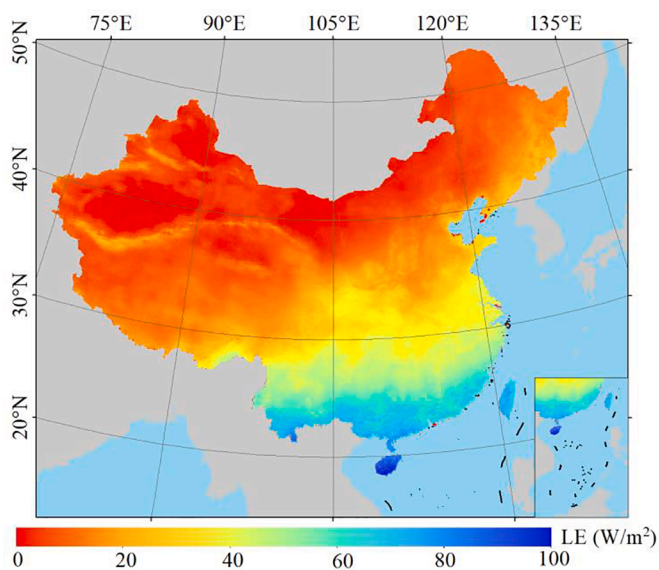

Fig. 13. The spatial distribution of the annual mean LE of mainland China during 2006–2008.

temperature causing uncertainty in H and then encapsulation into LE. The sensitivity experiment indicates that TSLEM decreases the uncertainty caused by LST. The 3 K error in LST could cause a 30% LE estimation error in TSEB but only cause a 6% error in TSLEM in arid regions (Fig. 11).

Additionally, we improve LST decomposition from two procedures by (i) considering the effect of interception water on LST; and (ii) simplifying the aerodynamic resistance parameterization scheme. Considering interception water in the TSLEM improved the performance of LST decomposition, especially in areas with sufficient rainfall (Figs. 4 and 5). This may be explained by the fact that rainfall intercepted by land surface can alter LST by absorbing partly energy. The aerodynamic resistance parameterization scheme adopted in TSEB is slightly more accurate than that of TSLEM (Figs. 4 and 5). However, the parametrization scheme of TSEB is complex, and force variables WS from meteorological reanalysis data bear great uncertainty. Therefore, to reduce the effects of WS on LE models and simplify the r_a parameterization process, we employ the scheme adopted in TSLEM rather than TSEB to decompose LST.

The limitation of SM on LE in the PT-JPL model is solely dependent on meteorological data. The coarse resolution of meteorological data hinder the PT-JPL model for mapping the spatial variability of SM constraints on LE, especially for the water-limited heterogeneous land surfaces (Purdy et al., 2018; Yang et al., 2015). LST is a distinctive signature of SM, with low/high LST generally indicating wet/dry SM

conditions (Dong et al., 2016; Sandholt et al., 2002). In our model, an all-weather satellite LST product with a 1 km spatial resolution was used to detect the variation in SM. We utilized the PM equation instead of PT to estimate LE_c and LE_s because it considers the effect of atmospheric moisture deficit on LE.

5.2. Model uncertainties

Despite our model has improved the model performance and decreased the sensitivity to input variables, the estimated LE still remains uncertain. This uncertainty mainly comes from errors of input variables, missing LE simulation processes, and spatial mismatch among different data sources.

(1) Error of input variables. The errors of input variables, including satellite-based blending LST, LAI/f_c, and meteorological data MERRA-2, all can contribute to the uncertainties of LE estimation. The all-weather LST product used in our study is obtained from the blending of PMW and MODIS LST products. Duan et al. (2017) reported that the RMSE of blending LST under cloudy conditions varied from 3.5 K to 4.4 K. Sensitivity analysis shows that bias in blending LST may cause 6–8% LE estimation errors in arid regions (Fig. 11). To generate the daily LE product, 8-day LAI/f_c was linearly interpolated to daily. However, the variations in LAI/f_c within 8 days were not linear. Many previous studies found that MERRA-2 product has large biases. For instance, Zhang et al. (2020) reported the bias of MERRA-2 R_s ranges from 35.68 to 43.84 W/m^2. In the current study, R_n is calculated as the sum of R_s and R_l. The overestimate in R_s will be linearly transferred to LE (Fig. 11).

(2) Missing LE simulation process. It is a challenge to simulate all LE-related processes because the process of evapotranspiration is affected by numerous physical factors, including biophysics, plant species, meteorological factors, and other factors. Therefore, simplifying LE process may lead to partial bias of LE estimation. For example, CO_2 can influence plant transpiration because high CO_2 induces stomatal closure (Idso and Brazel, 1984; Mu et al., 2011; Yao et al., 2013). This may lead to the overestimation of LE because our model ignores the effects of CO_2 on LE. The retrieval of global CO_2 from the TanSat satellite (Hong et al., 2021; Wang et al., 2020) is an opportunity to add the effect of enriched CO_2 into the LE model.

(3) Spatial mismatch among different data sources. The spatial resolution of satellite-based $f_c/LAI/LST$ is 1 km while the resolution of MERRA-2 data is 0.5°. To match with satellite data, the MERRA-2 data were spatially interpolated from 0.5° to 1 km. However, meteorological conditions can vary significantly within 0.5° as the heterogeneity of vegetation and terrain. Therefore, the process of resampling and spatial mismatch among different data sources may introduce errors and contribute to the uncertainty of LE estimation. Future studies should explore reducing the use of meteorological forcing to further decrease the influence of spatial mismatch on LE estimation (El Masri et al., 2019).

5.3. Merits and limitations of TSLEM

Compared with other models, TSLEM has four advantages. First, TSLEM considers the effect of interception water in LST decomposition and uses NDTI calculated from decomposed soil skin temperature to parameterize r_s in the PM equation. Our scheme minimizes the LE biases caused by LST errors. Second, TSLEM requires relatively fewer variables (LST, R_n, NDVI, RH, P_a, and T_a) that can be obtained from satellite and reanalysis meteorological data at the regional or global scale. Third, TSLEM is a robust LE model based on the sensitivity experiment. R_n, T_a, and RH are the main error sources of TSLEM that can be easily obtained with reasonable accuracy. Finally, TSLEM simplifies the process for

aerodynamic resistance in the TSEB model and therefore reduces the required forcing variables, which produce comparable accuracy of LST decomposition when compared with the widely used TSEB model.

Like many TSEB models, TSLEM has three limitations. First, TSLEM requires instantaneous meteorological data (T_a, R_n, and RH) at the time of TIR-derived LST acquisition, which may not be routinely accessed in some datasets. To expand the available data, the data interpolation methods introduced by McVicar and Jupp (1999) can be used to convert daily data into special time-of-day. Second, the assumption of an inverse relationship between NDTI and r_s based on statistical analysis may be problematic. The relationship between NDTI and r_s is complex, and it is a challenge to accurately describe the relationship between them with a simple mathematical formula. The mathematical relationship between them requires future research and is beyond the scope of this study. Finally, TSLEM adopts the same parameters over different vegetation types. However, for different vegetation types, differences in these parameters may be more reasonable.

6. Conclusion

This study developed a novel TIR-derived three-source LE model (TSLEM) for LE estimation, which could generate accurate LE estimation under all-sky conditions with few forcing data. In our model, LE was composed of heat flux from soil evaporation, canopy transpiration and interception water evaporation, and calculated by Penman-Monteith (PM) model, simplified MOD16 algorithm and Priestley-Taylor method, respectively. Importantly, the land surface temperature is decomposed into soil temperature, canopy temperature and interception water temperature by a new strategy. And then the soil resistance in PM model is parameterized by normalized difference temperature index (NDTI) derived from T_s. This novel LE model is capable of mapping the spatial variability of soil evaporation controlled by soil moisture.

The model was validated and compared with three LE models (PT-JPL, TSEB, and DSLEM) at 26 EC sites representing 8 vegetation types across mainland China. The validation and comparison illustrated that TSLEM yielded comparable accuracy with few forcing data. Large uncertainty in the TSEB model from the use of LST has been decreased in our model. Missing the effect of interception water is responsible for the underestimation of DSLEM. The PT-JPL model systematically underestimated LE in many EC sites of arid regions, and great uncertainties exist in TSEB estimated LE.

TSLEM provides a new operational method for derivation of all-sky daily LE on a regional scale using all-weather LST, which are significant interest for monitoring both the effects of soil and atmosphere moisture on LE. An important next step is to assess the application potential of TSLEM in agriculture, ecology and hydrology. Furthermore, improving the accuracies of meteorological and satellite-derived input variables is beneficial for decreasing the uncertainties of all-sky daily LE and should be explored in the future studies.

Declaration of Competing Interest

The authors declare that they have no known competing financial interests or personal relationships that could have appeared to influence the work reported in this paper.

Supplementary materials

Supplementary material associated with this article can be found, in the online version, at doi:10.1016/j.agrformet.2022.109066.

References

Anderson, M.C., Norman, J.M., Diak, G.R., Kustas, W.P., Mecikalski, J.R., 1997. A two-source time-integrated model for estimating surface fluxes using thermal infrared remote sensing. Remote Sens. Environ. 60 (2), 195–216.

Anderson, M.C., Norman, J.M., Mecikalski, J.R., Otkin, J.A., Kustas, W.P., 2007. A climatological study of evapotranspiration and moisture stress across the continental United States based on thermal remote sensing: 1. Model formulation. J. Geophys. Res-Atmos. 112 (D10).

Asdak, C., Jarvis, P.G., van Gardingen, P., Fraser, A., 1998. Rainfall interception loss in unlogged and logged forest areas of Central Kalimantan. Indonesia. J. Hydrol. 206 (3–4), 237–244.

Baldocchi, D., et al., 2001. FLUXNET: a new tool to study the temporal and spatial variability of ecosystem-scale carbon dioxide, water vapor, and energy flux densities. B Am. Meteorol. Soc. 82 (11), 2415–2434.

Brust, C., et al., 2021. Using SMAP Level-4 soil moisture to constrain MOD16 evapotranspiration over the contiguous USA. Remote Sens. Environ. 255.

Carlson, T.N., Gillies, R.R., Perry, E.M., 1994. A method to make use of thermal infrared temperature and NDVI measurements to infer surface soil water content and fractional vegetation cover. Remote Sensing Rev. 9 (1), 161–173.

Choudhury, B.J., et al., 1998. A biophysical process-based estimate of global land surface evaporation using satellite and ancillary data - II. Regional and global patterns of seasonal and annual variations. J. Hydrol. 205 (3–4), 186–204.

Cleugh, H.A., Leuning, R., Mu, Q.Z., Running, S.W., 2007. Regional evaporation estimates from flux tower and MODIS satellite data. Remote Sens. Environ. 106 (3), 285–304.

Colaizzi, P.D., et al., 2014. Two-source energy balance model to calculate E, T, and Et: comparison of priestley-taylor and penman-monteith formulations and two time scaling methods. T Asabe 57 (2), 479–498.

Colaizzi, P.D., et al., 2012. Two-source energy balance model estimates of evapotranspiration using component and composite surface temperatures. Adv. Water Resour. 50, 134–151.

Dong, J.Z., Steele-Dunne, S.C., Ochsner, T.E., van de Giesen, N., 2016. Determining soil moisture and soil properties in vegetated areas by assimilating soil temperatures. Water Resour. Res. 52 (6), 4280–4300.

Duan, S.B., Li, Z.L., Leng, P., 2017. A framework for the retrieval of all-weather land surface temperature at a high spatial resolution from polar-orbiting thermal infrared and passive microwave data. Remote Sens. Environ. 195, 107–117.

El Masri, B., Rahman, A.F., Dragoni, D., 2019. Evaluating a new algorithm for satellite-based evapotranspiration for North American ecosystems: model development and validation. Agr. Forest Meteorol. 268, 234–248.

Fisher, J.B., et al., 2009. The land-atmosphere water flux in the tropics. Global Change Biol. 15 (11), 2694–2714.

Fisher, J.B., et al., 2017. The future of evapotranspiration: global requirements for ecosystem functioning, carbon and climate feedbacks, agricultural management, and water resources. Water Resour. Res. 53 (4), 2618–2626.

Fisher, J.B., Tu, K.P., Baldocchi, D.D., 2008. Global estimates of the land-atmosphere water flux based on monthly AVHRR and ISLSCP-II data, validated at 16 FLUXNET sites. Remote Sens. Environ. 112 (3), 901–919.

Fisher, J.B., Whittaker, R.J., Malhi, Y., 2011. ET come home: potential evapotranspiration in geographical ecology. Global Ecol. Biogeogr. 20 (1), 1–18.

Fu, B.J., et al., 2010. Chinese ecosystem research network: progress and perspectives. Ecol. Complex 7 (2), 225–233.

Gelaro, R., et al., 2017. The modern-era retrospective analysis for research and applications, version 2 (MERRA-2). J. Climate 30 (14), 5419–5454.

Hong, X. et al., 2021. Retrieval of global carbon dioxide from tansat satellite and comprehensive validation with TCCON measurements and satellite observations. PP (99): 1–16.

Idso, S.B., Brazel, A.J., 1984. Rising atmospheric carbon-dioxide concentrations may increase streamflow. Nature 312 (5989), 51–53.

Jackson, R.D., Idso, S.B., Reginato, R.J., Pinter, P.J., 1981. Canopy temperature as a crop water-stress indicator. Water Resour. Res. 17 (4), 1133–1138.

Jia, K., et al., 2015. Global land surface fractional vegetation cover estimation using general regression neural networks from MODIS surface reflectance. Ieee T Geosci. Remote 53 (9), 4787–4796.

Kalma, J.D., McVicar, T.R., McCabe, M.F., 2008. Estimating land surface evaporation: a review of methods using remotely sensed surface temperature data. Surv. Geophys. 29 (4–5), 421–469.

Kustas, W.P., Daughtry, C.S.T., 1990. Estimation of the soil heat flux/net radiation ratio from spectral data. Agr. Forest Meteorol. 49 (3), 205–223.

Kustas, W.P., Norman, J.M., 1999. Evaluation of soil and vegetation heat flux predictions using a simple two-source model with radiometric temperatures for partial canopy cover. Agr. Forest Meteorol. 94 (1), 13–29.

Li, Z.L., et al., 2009. A review of current methodologies for regional evapotranspiration estimation from remotely sensed data. Sensors-Basel 9 (5), 3801–3853.

Liang, S.L., et al., 2021. The global land surface satellite (GLASS) product suite. B Am. Meteorol. Soc. 102 (2), E323–E337.

Liu, S.M., et al., 2011. A comparison of eddy-covariance and large aperture scintillometer measurements with respect to the energy balance closure problem. Hydrol. Earth Syst. Sc. 15 (4), 1291–1306.

Liu, S.M., Xu, Z.W., Zhu, Z.L., Jia, Z.Z., Zhu, M.J., 2013. Measurements of evapotranspiration from eddy-covariance systems and large aperture scintillometers in the Hai River Basin. China. J. Hydrol. 487, 24–38.

McVicar, T.R., Jupp, D.L.B., 1998. The current and potential operational uses of remote sensing to aid decisions on drought exceptional circumstances in Australia: a review. Agr. Syst. 57 (3), 399–468.

McVicar, T.R., Jupp, D.L.B., 1999. Estimating one-time-of-day meteorological data from standard daily data as inputs to thermal remote sensing based energy balance models. Agr. Forest Meteorol. 96 (4), 219–238.

Moran, M.S., Clarke, T.R., Inoue, Y., Vidal, A., 1994. Estimating crop water-deficit using the relation between surface-air temperature and spectral vegetation index. Remote Sens. Environ. 49 (3), 246–263.

Mu, Q., Heinsch, F.A., Zhao, M., Running, S.W., 2007. Development of a global evapotranspiration algorithm based on MODIS and global meteorology data. Remote Sens. Environ. 111 (4), 519–536.

Mu, Q.Z., Zhao, M.S., Running, S.W., 2011. Improvements to a MODIS global terrestrial evapotranspiration algorithm. Remote Sens. Environ. 115 (8), 1781–1800.

Norman, J.M., Kustas, W.P., Humes, K.S., 1995. Source approach for estimating soil and vegetation energy fluxes in observations of directional radiometric surface-temperature. Agr. Forest Meteorol. 77 (3–4), 263–293.

Pastorello, G., et al., 2020. The FLUXNET2015 dataset and the ONEFlux processing pipeline for eddy covariance data. Sci. Data 7 (1).

Priestley, C.H.B., Taylor, R.J., 1972. On the assessment of surface heat flux and evaporation using large scale parameters. Mon. Weather Rev. 100 (2), 81–92.

Purdy, A.J., et al., 2018. SMAP soil moisture improves global evapotranspiration. Remote Sens. Environ. 219, 1–14.

Rowe, L.K., 1983. Rainfall interception by an evergreen beech forest, nelson, New-Zealand. J. Hydrol. 66 (1–4), 143–158.

Sandholt, I., Rasmussen, K., Andersen, J., 2002. A simple interpretation of the surface temperature/vegetation index space for assessment of surface moisture status. Remote Sens. Environ. 79 (2–3), 213–224.

Schimel, D., et al., 2019. Flux towers in the sky: global ecology from space. New Phytol. 224 (2), 570–584.

Stewart, J.B., et al., 1994. Sensible heat flux-radiative surface temperature relationship for 8 semi-arid areas. J. Appl. Meteorol. 33 (9), 1110–1117.

Stone, P.H., Chow, S., Quirr, W.J., 1977. July climate and a comparison of january and july climates simulated by giss general circulation model. Mon. Weather Rev. 105 (2), 170–194.

Su, Z., 2002. The surface energy balance system (SEBS) for estimation of turbulent heat fluxes. Hydrol. Earth Syst. Sc. 6 (1), 85–99.

Sugita, M., Brutsaert, W., 1991. Daily evaporation over a region from lower boundary-layer profiles measured with radiosondes. Water Resour. Res. 27 (5), 747–752.

Tang, R.L., Li, Z.L., Tang, B.H., 2010. An application of the T-s-VI triangle method with enhanced edges determination for evapotranspiration estimation from MODIS data in and and semi-arid regions: implementation and validation. Remote Sens. Environ. 114 (3), 540–551.

Timmermans, W.J., Kustas, W.P., Anderson, M.C., French, A.N., 2007. An intercomparison of the surface energy balance algorithm for land (SEBAL) and the two-source energy balance (TSEB) modeling schemes. Remote Sens. Environ. 108 (4), 369–384.

Twine, T.E., et al., 2000. Correcting eddy-covariance flux underestimates over a grassland. Agr. Forest Meteorol. 103 (3), 279–300.

Verhoef, A., DeBruin, H.A.R., VandenHurk, B.J.J.M., 1997. Some practical notes on the parameter kB(-1) for sparse vegetation. J. Appl. Meteorol. 36 (5), 560–572.

Wang, S.P., et al., 2020. Carbon dioxide retrieval from tansat observations and validation with TCCON measurements. Remote Sens-Basel 12 (14).

Wang, Y.P., et al., 2019. A three-source satellite algorithm for retrieving all-sky evapotranspiration rate using combined optical and microwave vegetation index at twenty AsiaFlux sites. Remote Sens. Environ. 235.

Xiao, Z.Q., et al., 2014. Use of general regression neural networks for generating the GLASS leaf area index product from time-series MODIS surface reflectance. Ieee T. Geosci. Remote 52 (1), 209–223.

Xu, S., Cheng, J., 2021. A new land surface temperature fusion strategy based on cumulative distribution function matching and multiresolution Kalman filtering. Remote Sens. Environ. 254.

Yang, Y.T., et al., 2015. Comparison of three dual-source remote sensing evapotranspiration models during the MUSOEXE-12 campaign: revisit of model physics. Water Resour. Res. 51 (5), 3145–3165.

Yao, Y.J., et al., 2018. Satellite detection of water stress effects on terrestrial latent heat flux with MODIS shortwave infrared reflectance data. J. Geophys. Res-Atmos. 123 (20), 11410–11430.

Yao, Y.J., et al., 2013. MODIS-driven estimation of terrestrial latent heat flux in China based on a modified Priestley-Taylor algorithm. Agr. Forest Meteorol. 171, 187–202.

Yao, Y.J., et al., 2017a. Estimation of high-resolution terrestrial evapotranspiration from Landsat data using a simple Taylor skill fusion method. J. Hydrol. 553, 508–526.

Yao, Y.J., et al., 2017b. A simple temperature domain two-source model for estimating agricultural field surface energy fluxes from Landsat images. J. Geophys. Res-Atmos. 122 (10), 5211–5236.

Yu, G.R., et al., 2006. Overview of ChinaFLUX and evaluation of its eddy covariance measurement. Agr. Forest Meteorol. 137 (3–4), 125–137.

Zhan, X., Kustas, W.P., Humes, K.S., 1996. An intercomparison study on models of sensible heat flux over partial canopy surfaces with remotely sensed surface temperature. Remote Sens. Environ. 58 (3), 242–256.

Zhang, K., Kimball, J.S., Nemani, R.R., Running, S.W., 2010. A continuous satellite-derived global record of land surface evapotranspiration from 1983 to 2006. Water Resour. Res. 46.

Zhang, X.X., Lu, N., Jiang, H., Yao, L., 2020. Evaluation of reanalysis surface incident solar radiation data in China. Sci. Rep-Uk 10 (1).

Zhao, W.L., et al., 2020. Uncertainties caused by resistances in evapotranspiration estimation using high-density eddy covariance measurements. J. Hydrometeorol. 21 (6), 1349–1365.

Zhou, Z.Q., et al., 2021. Characteristics of propagation from meteorological drought to hydrological drought in the pearl river basin. J. Geophys. Res-Atmos. 126 (4).

Zhou, Z.Q., et al., 2020. Assessing spatiotemporal characteristics of drought and its effects on climate-induced yield of maize in Northeast China. J. Hydrol. 588.